

Influence of imidazole functionalization on the properties of small molecule models of the LPMO active site†

Ugo Gilbert^a, Xiao Mu^a, Yan Yu Sarah Lam^a, Gaël De Leener^b, Maëlle Bottin^a, Koen Robeyns^a, Michel Luhmer^b, Raphaël Robiette^a, Michael L. Singleton^{a*}

^a Molecular Chemistry, Materials and Catalysis Division, Institute of Condensed Matter and Nanosciences, Université catholique de Louvain, Place Louis Pasteur 1, Louvain-la-Neuve, 1348, Belgium.

^b Université libre de Bruxelles - ULB, Faculté des Sciences, Laboratoire de Résonance Magnétique Nucléaire Haute Résolution & Centre d'Instrumentation en Résonance Magnétique - CIREM, Avenue F.D. Roosevelt, 50, CP 160/08, 1050 Brussels, Belgium.

*Email: m.singleton@uclouvain.be

ABSTRACT: A series of small molecule Cu(II) complexes based on tridentate N₃ ligands relevant to the histidine brace of the active site of lytic polysaccharide monooxygenase were synthesized and characterized by X-ray crystallography and spectroscopic studies. In order to better understand the role of different structural features and to help bridge the differences between previously reported models, the methylation patterns, imidazole connectivity, linker nature, and type of heterocycle were systematically varied across the series. These modifications lead to important differences in the electrochemical properties of the complexes and their reactivity towards the oxidation of a model substrate.

Introduction

Lytic polysaccharide monooxygenases (LPMO) are a family of copper containing metalloenzymes important for biofuel and sustainable commodity chemical production due to their ability to enhance recalcitrant polysaccharide degradation through the oxidative cleavage of strong glycosidic C-H bonds.^{1–4} The active site of LPMO consists of a single copper atom bound in a T-shaped N₃ coordination environment, referred to as the histidine brace, which is comprised of the imidazole and primary amine of an N-terminal histidine and a second histidine imidazole, **Figure 1A–B**.^{5,6} In some members of the LPMO family, the imidazole of the N-terminal histidine is N-methylated. The origin and the impact of this modification is still unknown. It has been suggested to protect against oxidative damage, but computational studies suggest it does not impact the mode of action of the histidine brace.^{7,8} Further variation in exogenous ligands or second-coordination sphere residues between different LPMO have also been reported.^{6,9,10} Still, the core histidine brace is conserved across all members of the LPMO family and is proposed to be important for the high reactivity of these enzymes. This has made it an intriguing structure for study with synthetic complexes, both to aid in understanding of the structural features important for reactivity and for the possibility to develop new synthetic catalysts capable of similar reactivity.

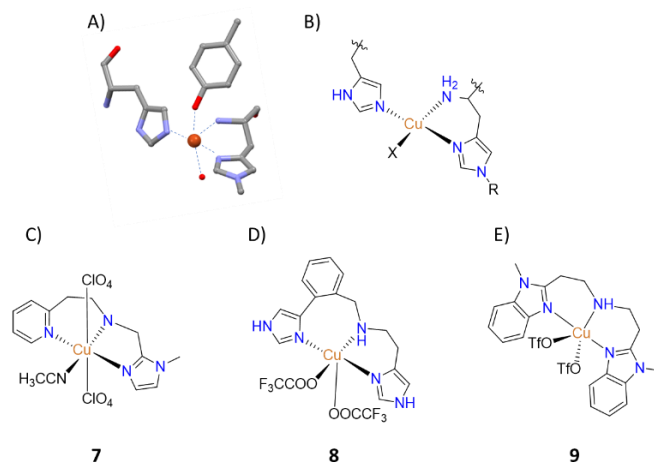


Figure 1: A) Structure of the active site of LPMO taken from PDB(4ALC)¹¹. B) Schematic structures of the LPMO histidine brace, and reported model complexes (C–E).

Nevertheless, despite the apparent simplicity of the histidine brace motif, only a limited number of imidazole containing structural models have been reported so far.^{12–25} The Castillo and Simaan groups reported some of the earliest LPMO models using tridentate ligands comprised of either benzimidazoles or one imidazole and one pyridine connected through an aliphatic linker containing a secondary amine (**Figure 1C and E**).^{26–29} These structures were able to provide a similar N₃ coordination environment as in the natural system and further showed oxidative reactivity towards saccharide substrates in the presence of hydrogen peroxide. Later, Itoh and coworkers, in order to more accurately mimic the imidazoles found in the histidine brace, designed a ligand containing two imidazole rings connected in the 4-position by an alkylamine (**Figure 1D**).³⁰ Their model mimics both the N₃ environment around the copper and better emulates the large dihedral angle between

the histidine imidazoles in the enzyme (>50°), a feature they proposed as important for the properties and reactivity of LPMOs. Their system provides not only a good match for the physicochemical properties, in particular the high Cu(II)/Cu(I) reduction potential observed in the natural system but also showed high reactivity toward oxidation of a model saccharide substrate and cyclohexane in presence of hydrogen peroxide making it the best model to date for LPMOs.

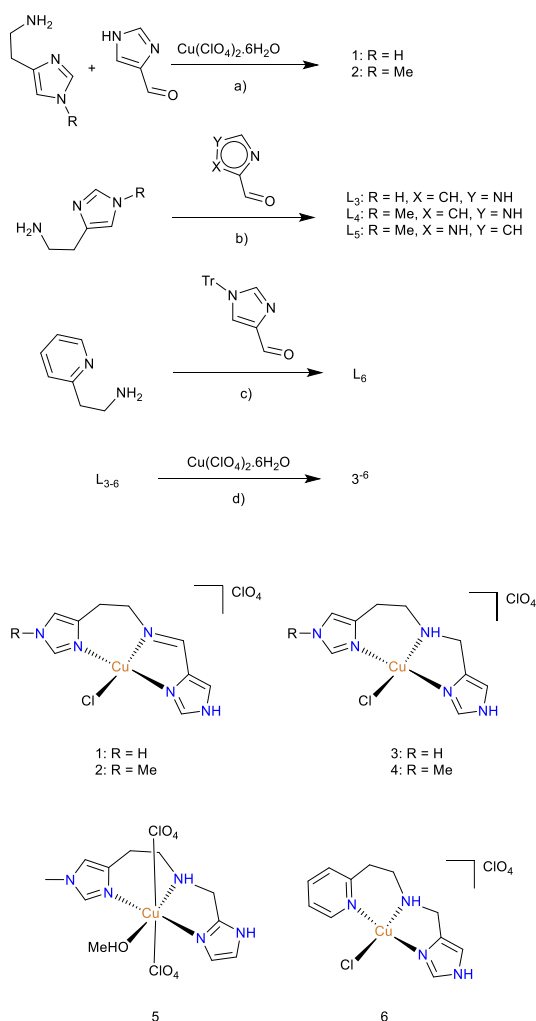
Still structural models of the active site are rare, especially those containing 4- or 5-position connected imidazole units as found in nature, and substantial structural variation (methylation patterns, linker, and heterocycles used) between the reported complexes makes comparison and identification of the effects of different structural features important for the histidine brace reactivity and properties difficult.

In this work, we describe the synthesis, characterization, and reactivity of a series of small molecule copper complexes, (**Scheme 1**), based on tridentate N₃ ligands composed of two trans imidazoles and an alkylamine linker, mimicking the histidine brace motif of LPMOs. Six new complexes with systematic variation of the imidazole methylation patterns, the connectivity of the imidazole rings, the imine vs amine character of the central N-donor group, and the type of heterocycle present were obtained. Their structures and electrochemical properties were studied along with their oxidative reactivity towards a model saccharide substrate, allowing to determine the impact of different structural modifications on their physicochemical and catalytic properties.

Results and discussion

Synthetic routes for complexes **1-6** are shown in **Scheme 1**. The imine complexes **1** and **2** were synthesized in one step through copper templated imine formation by reaction of imidazole-4-carboxaldehyde with the HCl salts of either 1-Me or 1-H histamine in the presence of Cu(ClO₄)₂ (**Caution!** Copper perchlorate is a category 2 oxidizing solid and potentially explosive. Precautions should be taken with its handling.) in methanol and isolated by filtration (**Schemes 1, S5** and **S6**). The amine ligands were synthesized by reductive amination using histamine or 1-methylhistamine^{31,32} and imidazole 2-carboxaldehyde or trityl protected imidazole 4-carboxaldehyde³³ in dry methanol in the presence of 3 Å activated molecular sieves (**Schemes S1 – S4** and **S7 – S14**). The imine intermediate was observed by NMR but was not isolated due to its low stability. While the direct reduction with sodium borohydride gave **L5** in its neutral form in a good yield, for **L3**, **L4**, and **L6** the tritylated counterpart of the aldehyde was used for the reductive amination to facilitate synthesis and purification. The deprotection of the trityl group was performed quantitatively under aqueous acidic conditions and gave **L3**, **L4**, and **L6** as their HCl salts in moderate to good overall yields. Complexes **3-6** were then synthesized by adding Cu(ClO₄)₂ to a methanol solution of the corresponding ligand followed by

precipitation with diethyl ether to give the crude complexes as blue powders (**Schemes S15 – S19**). The solids were then purified by crystallization using vapor diffusion of ether into a solution of the complex in methanol to give **3-5** in 20-50% yield.



Scheme 1: Synthesis of ligands **L3-6** and complexes **1-6**. a) MeOH/r.t./overnight. b) i: NaOH/NaBH₄/MeOH/r.t./4h, ii (if trityl): HCl 35%/r.t./overnight c) i: NaOAc/NaBH₄/MeOH/r.t./6h, ii: HCl 35%/r.t./overnight. d) MeOH/r.t./overnight.

This crystalline material was used for all analyses. To have a comparison with the literature, complex **7** reported by Simaan and co-workers,²⁸ containing a pyridine moiety and a 2-position connected imidazole, was resynthesized following the same procedure as for **3-6** (**Scheme S20**).

Solid State structures of 1-6

X-ray quality crystals of **1-6** and trityl derivative **3^{Tr}** were obtained as described above. The crystal structures are shown in **Figure 2** and important geometric parameters are listed in **Table 1**. In all cases, the ligands are coordinated to a single Cu

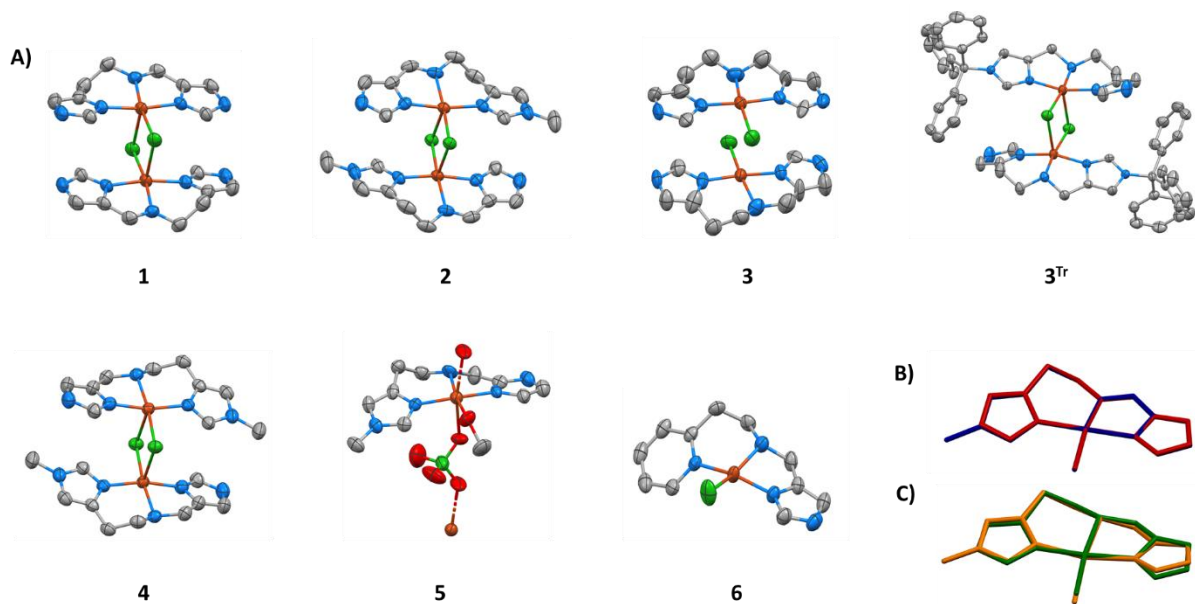


Figure 2: A) ORTEP representations of complexes **1-6** and **3Tr** with displacement ellipsoids drawn at the 50% occupancy level; Hydrogen atoms and non-coordinated perchlorate counterions are omitted for clarity. B) Overlaid structures of **1** (red) and **2** (blue). C) Overlaid structures of **3** (green) and **4** (orange).

center in a tridentate fashion through the two imidazoles and the amine nitrogen of the linker, giving a T-shaped N₃ coordination environment similar to what is observed in LPMO and in previously reported complexes (**7-9**).

Consistent with the elemental analyses, structures **1-4** and **6** contain one free perchlorate counterion and a chloride,

position and two perchlorate counterions, one free and one axially bound, similar to what is described for the pyridine/2-position imidazole complex. The ranges for the Cu-N_{imid} and Cu-N_{linker} distances are 1.92-1.97 Å and 2.04-2.07 Å respectively. The two cis N_{imid}-Cu-N_{linker} angles vary expectedly with chelate ring size and measures on average 92.5° on the side of the six-

Table 1: Comparison of the structural properties for compounds **1-7** and LPMO active site.

Compound	Cu-N _{imid} (Å)	Cu-N _{linker} (Å)	N-Cu-N _{trans} (°)	N-Cu-N _{cis} (°)	Heterocycle angle ^b (°)
1	1.95	2.04	170.9	91.5, 80.9	15.8
2	1.95, 1.97	2.04	170.4	91.6, 80.8	15.1
3	1.92, 1.97	2.05	174.2	94.5, 79.7	3.7
3Tr	1.95	2.09	164.6	92.8, 80.4	42.7
4	1.96	2.07	167	92.3, 80.2	22.3
5	1.93, 1.95	2.06	174.2	94.3, 82.2	28.1
6	1.94, 1.98 ^a	2.02	161	95.1, 81.2	41.8 ^c
7 ²⁸	1.97, 2.02 ^a	2.04	170.2	95.9, 81.5	33.4
8 ³⁰	1.97	2.06	173.4	93.2, 91	75.6
9 ²⁶	1.97	2.13	175.4	92.3	2.4
LPMO ^{11,35-37}	1.87 - 2.09	2.01 - 2.29	153 - 176.5	106.9 - 87.1	58.1 - 67.4

^aDistance for Cu-Pyridine, ^bHeterocycle angle is the measured angle between planes made by the atoms of each heterocyclic ring. ^cMean angle calculated on the disordered structures.

originating from the starting HCl salt of the ligand, bound in the fourth equatorial position. By contrast, complex **5**, in which one imidazole is connected to the linker through the 2-position of the ring, has a methanol molecule bound in the equatorial

membered chelate ring and 80.4° on the side of the 5-membered chelate ring. Globally, the related pairs of compounds (amine versus imine linkers) exhibit nearly identical structural parameters. Notably, the N-methylation of the

imidazole does not appear to have a substantial impact on the copper structural environment. The same is true for the imidazole connectivity. The distances and angles observed for complex **5** were comparable to the 4-position imidazole derivatives.

Complexes **1**, **2**, and **4** form discrete dimers in the solid state as a result of interactions of the coordinated chlorides with the metal center of a neighboring complex. The average Cu-Cl distances for the equatorially coordinated chloride is 2.3 Å, while the distance to the chloride of the neighboring complex is 2.8 Å, with the Cl-Cu-Cl' angles ranging between 96-98°. The relatively long distances for the axial chloride interaction suggest that the structures are weakly held together. In related axial chloride bridged copper dimers, dissociation has been shown to occur in protic solvents, with the chlorides being replaced by solvent^{37,38}. The weak interaction with chloride is further seen in complex **3**. In contrast to **1**, **2**, and **4**, complex **3** forms extended 1-D coordination polymers in the solid state with longer distances (3.1-3.3 Å) between the copper centers and the neighboring chlorides and a potential hydrogen bonding interaction between the bound chloride and the amine N-H of an adjacent complex. Considering the 5-coordinate N3ClCl' Cu centre, τ_5 calculated for structures **1-4** is close to 0 (between 0.005 and 0.09), indicating a near perfect square pyramidal arrangement around the copper^{39,40}. Like **3**, complex **5** also forms a 1-D coordination polymer. The axially bound perchlorate ion bridges between adjacent copper sites (Cu-O \approx 2.52 Å) resulting in a Cu-Cu separations of 7.26 Å and a distorted octahedral geometry around the copper. Interestingly, compound **6** appears as a monomeric copper complex. The coordinating chloride does not show any direct interaction with neighboring copper centers and is oriented towards the linker N-H of adjacent complexes, allowing for potential weak hydrogen bonding interactions (N-Cl 3.204 Å) in the solid state, though it should be noted that the N-H is disordered, with a minor part instead engaged in a hydrogen bond with a nearby perchlorate ion. This leads to a close packing of the complexes that results in substantial disruption of the square pyramidal geometry. The pyridine ring deviates from the ligand plane (angle between both heterocyclic rings is 46.6°) giving a trans Npyr-Cu-Nimid angle of about 161° ($\tau_4' = 0.28$) with a distorted square planar geometry.

The differences in packing appear to have an important effect on the angle between the two heterocyclic rings, a structural parameter recently proposed to be potentially related to the electrochemical properties and high reactivity observed in natural LPMO³⁰. Consistent with their more rigid structures, resulting from the imine group, the angles between the planes of the heterocycles for complexes **1** and **2** are similar, 15.8° and 15.1° respectively. Greater variation is observed with the more flexible systems **3-5**. While in **4** and **5**, larger angles are observed (22.3° for **4** and 28.1° for **5**), in complex **3** the angle is only 3.7°. This much smaller value appears to be due to close stacking of the imidazole rings between adjacent structures in the 1-D chains. In **4** and **5**, the complexes are staggered providing more freedom for the imidazole rings. The DFT optimized structures of the monomeric forms of **3-5** (see supporting information and

figure S50) showed angles similar for all three complexes (28.6 – 32.4°) and larger than the values observed in the solid state. Compound **6** displays the highest heterocycle angle of the series with a value of 46.6°. This is explained by the more distorted structure and the pyridine ring deviating from the ligand plane. The flexible nature of the linkers and imidazole units can also be seen in compound **3^{Tr}** containing the bulky trityl group. Surprisingly, this complex also forms dimers in the solid phase, with the flexibility of the structure helping to minimize steric clash between the two units by adopting more of a butterfly shape ($\tau_5 = 0.15$).

Solution studies

The long-range axial Cu-Cl distances observed for **1-4** in the solid state and the known propensity for chlorides in cis-dichloro copper complexes to be exchanged for solvent in aqueous or methanolic solutions,^{41,42} suggest that the dimers observed for these complexes are weakly bound. In solution, it is expected that they dissociate to give the mononuclear species. Indeed, the electron paramagnetic resonance (EPR) spectra of all complexes, recorded in frozen methanolic solution at 100 K, exhibit axial signals with $g_{||} > g_{\perp}$, consistent with a mononuclear Cu(II) complex coordinated in a distorted square pyramidal geometry^{28,30,38} (**Table 2, Figures S9 – S14**). Further, the g -tensor and hyperfine coupling values obtained all fall into the range of values observed for LPMO and related monomeric copper complexes,^{17,38,43} suggesting similar structures and supporting that the aggregates present in the solid state for **1-4** dissociate to give the mononuclear complexes in solution.

Table 2: Summary of the EPR parameters.

Compound	$g_{ }$	g_{\perp}	$ A _{ }$ (G)	$ A _{\perp}$ (G)
1	2.271	2.059	157.3	13.9
2	2.267	2.060	158.2	13.2
3	2.260	2.068	164.8	16.0
4	2.254	2.060	159.9	12.2
5	2.266	2.064	154.7	19.8
6	2.268	2.063	164.2	9.9
LPMO ^{*,36}	2.226 - 2.28	g_x : 2.015 - 2.06 g_y : 2.052 - 2.116	116 - 186	$ A _x$: 3 - 42 $ A _y$: 0.5 - 50

*: Performed in aqueous solutions

UV absorption spectra (**Table 3, Figures S15 – S27**) were recorded for the complexes in aqueous solution. They all exhibit low intensity broad bands between 624 and 650 nm, typical of d-d transitions for copper (II) complexes in tetragonally distorted octahedral geometries, with weak axial solvent coordination^{41,42} and again similar to values reported for LPMO.^{24,26,28–30,36} The high intensity signals between 200 and 300 nm are assigned to $\pi \rightarrow \pi^*$ transition of the ligands and possibly to ligand to metal charge transfer (LMCT).⁴⁴ While methylation of the imidazoles does not lead to substantial changes, the λ_{max} of the d-d transition shows a bathochromic

shift of around 20 nm going from the amine to the imine complexes. A similar, though slightly smaller shift was noted for the 2-imidazole derivative complex **5** versus **3** and **4**. In both cases, imine or 2-imidazole, the changes are similar to what is observed when one imidazole is replaced by a pyridine unit. Solvent effects were studied by recording the spectra of **4-6** in acetonitrile and methanol (**4b** and **4c**). While methanol leads to spectra similar to those recorded in H₂O, MeCN leads to a hypsochromic shift of the d-d transitions. This variation may be attributed to the solvent interacting with the copper at the labile positions or potentially to the presence of a monomer/dimer equilibrium in MeCN. However, concentration studies on complexes **1-6** from 2 to 0.1 mM in the different solvents all show a linear response of the absorbance suggesting limited interaction between the complexes within this concentration range.

Table 3: Summary of the UV visible spectrometry characteristics.

Compound	Solvent	λ_{\max} [nm]	ϵ [L.mol ⁻¹ .cm ⁻¹]
1	H ₂ O	649	73
2	H ₂ O	650	73
3	H ₂ O	624	76
4	H ₂ O	633	49
4b	MeCN	611	87
4c	MeOH	627	95
5	H ₂ O	640	57
5b	MeCN	604	68
5c	MeOH	644	54
6	H ₂ O	647	79
6b	MeCN	641	129
6c	MeOH	654	132
7*	H ₂ O	649	72
8 ³⁰	MeOH	662	83
9 ²⁶	MeOH	723	157

*: Resynthesized

Electrochemistry

Electrochemical analysis of the compounds, performed in MeOH with tetrabutylammonium perchlorate (TBAClO₄) as the electrolyte, showed a single pseudo-reversible redox event between -542 to -464 mV vs ferrocene for all of the compounds (**1-6**), which is attributed to the Cu^{II}/Cu^I redox couple (Figures S28 – S35). Globally, these values are lower than those observed for reported models and LPMO^{26,28,30,36} (Table 4 Error! Reference source not found.). The reduction for the imine complexes is slightly higher than their amine counterparts (+23 mV and +24 mV for **1** and **2** respectively). Similarly, the 2-position connectivity of the imidazole, complex **5**, showed a 20 mV increase vs **4**. When comparing **1** and **3** versus **2** and **4**, the methylation shows only a small influence on the redox potential

with a difference between the methylated and non-methylated analogs being less than 10 mV. The introduction of a pyridine ring induced a substantial increase in the redox potential compared to the imidazole counterpart. **6** showed a 78 mV increase versus **4**, and the reported compound **7** showed a 76 mV gain over **5**. For this series, it appears that the electronic effects induced by changing the heterocycles are more prominent compared to other structural parameters in the first coordination sphere such as the electron-donating effect of methylation or the introduction of an imine function. Within the range of dihedral angles we observed, there was no strong correlation of this structural parameter with reduction potential.

Table 4: Summary of the electrochemical parameters.

Compound	MeOH		Phosphate Buffer
	E _{1/2} [mV]	ΔE [mV]	E _{red} [mV]
1	-524	139	-431
2	-518	109	-441
3	-547	147	-445
4	-542	95	-413
4 ^a	-650	128	/
5	-513	100	-394
5 ^a	-632	81	/
6	-464	116	-366
7 ^b	-437	87	-319

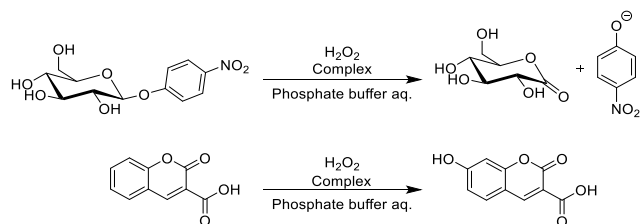
^a: TBACl as support electrolyte. ^b: Data recorded for the resynthesized compound.

To look at the influence of the counterions associated with the complexes in solution, electrochemical studies on compounds **4** and **5** were additionally performed with TBACl instead of TBAClO₄. Switching between non-coordinating ions, present in **5**, for the coordinating chloride ions, present in **4**, would be expected to have a larger effect on the redox potentials of **5**. However, the change for the two compounds is similar. The reduction potentials decrease by 108 for **4** and 119 mV for **5**. This implies that in MeOH solutions with non-coordinating counterions, the chlorides are largely replaced by solvent molecules or the ions from the electrolyte, and supports the other solutions studies which suggest that the dimers observed in the solid state are dissociated in solution.

Reactivity assays

The oxidative reactivity of the complexes **1-7** was tested using the p-nitrophenyl- β -D-glycopyranoside (PNPG) assay, Scheme 2.²⁸ These tests were conducted in a phosphate buffer (pH = 7.5) using 10 mM PNPG with 4 equivalents of H₂O₂ as the oxidant and a catalytic loading of 0.5 mol%.²⁹ The PNPG degradation was monitored by tracking the releases of the para-nitrophenolate. Under the conditions used, it is reported that roughly 75% of the para-nitrophenol is deprotonated giving the

characteristic absorption at 400 nm. It has been discussed in the literature that the produced para-nitrophenolate can undergo further degradation leading to an underestimation of product formation.²⁹



Scheme 2: (Top) Oxidative cleavage of p-nitrophenyl-β-D-glycopyranoside (PNPG). (Bottom) Coumarin-3-carboxylic acid (CCA) hydroxylation.

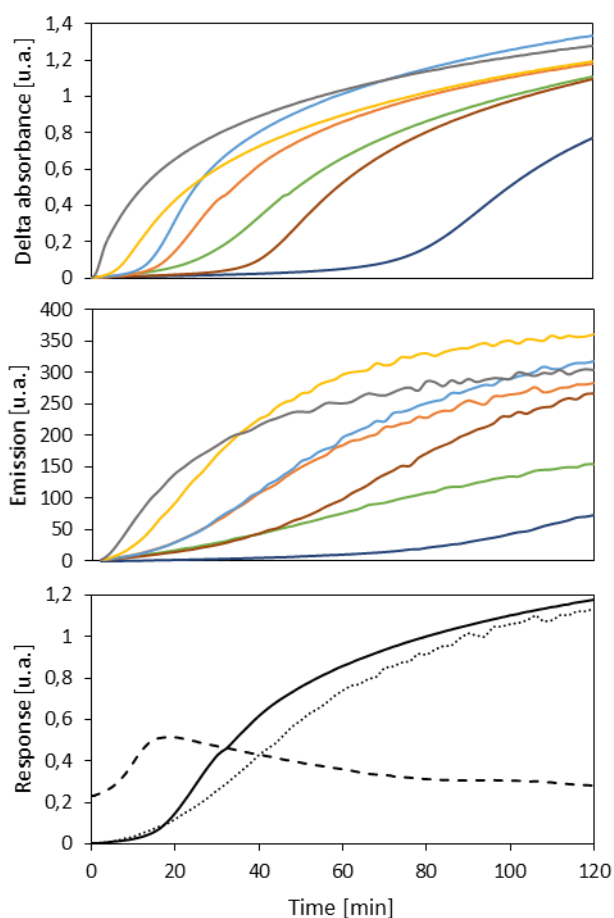


Figure 3: (Top) Evolution over time of *p*-nitrophenolate absorbance (at 400 nm) produced from the degradation of PNPG by the compounds **1** (dark blue), **2** (green), **3** (red), **4** (orange), **5** (light blue), **6** (yellow) and **7** (grey). (Center) Evolution over time of 7-hydroxycoumarin-3-carboxylic acid fluorescence (at 447 nm) produced from the hydroxy radical trap Coumarin-3-carboxylic acid with compound **1-7** (same colors as for Top). (Bottom) Comparison between the evolution over time of (dash line) the absorbance (at 305 nm) of the intermediate species after addition of 800 equivalents of H₂O₂, (plain line) *p*-nitrophenolate absorbance (at 400 nm) and (dots line) 7-hydroxycoumarin-3-carboxylic acid fluorescence (at 447 nm) for compound **4**.

All complexes tested in this paper show sigmoidal curves for product formation under the described conditions (Figure 3 top, S38 and S39). An induction period is observed during which no significant product is formed, followed by sudden substrate

degradation. The induction period varies from 3 minutes for complex 7 to 92 minutes for compound 1, and differs only a few minutes for each compound when the tests are repeated.

Table 5: Summary of the catalytic assays.

Compound	Time of Vmax [min]	Vmax [μM/min]	Yield ^b [%]	TON ^b
1	92	1.341	2.27	4.55
2	40	1.456	2.26	4.52
3	49	1.744	2.27	4.54
4	24	2.155	2.21	4.42
5	19	3.121	2.4	4.79
6	10	2.292	2.24	4.47
7^a	3	5.441	2.21	4.42
CuCl₂	/	/	2.16	4.13

^a: Resynthesized Complex. ^b: Calculated after 24h.

The time for the upsurge and the maximum production rate were obtained by taking the derivative of the evolution of the absorbance over time for each compound and data are presented in Table 5 (Figure S40). Complex 4, because of its moderate induction period was used to study the effects of catalyst and H₂O₂ concentration. Doubling the concentration of catalyst decreases the induction period by about half (12.5 minutes), while doubling the H₂O₂ concentration has a larger effect, decreasing by ~3/4 the time required to obtain the maximum rate (6.5 minutes) (Figure S41). Incubating the complex with the substrate, for 10 minutes or 1 hour, prior to H₂O₂ addition, did not lead to differences in the observed reactivity. However, adding H₂O₂ 20 or 60 minutes prior to PNPG substrate addition effectively removes the induction period, though waiting 60 minutes results in a substantial decrease in activity (Figure S43).

After 24h, the yield of the reaction with all complexes reaches around 2.2% which is comparable to other LPMO active site models tested on the same substrate. Most compounds produced roughly the same amount of chromophore after the reaction, which may be due to degradation of the complexes from auto-oxidation of the ligand. Indeed, after the initial upsurge, the slope of the product formation versus time becomes similar to that of the free copper salt. Adding another equivalent of catalyst or H₂O₂ to the catalytic assay after 1 hour leads to only a slight increase in nitrophenolate production, but rates observed after the initial induction period are not reobtained (Figure S42).

Relative to the structural modifications, it appears that the presence of an imine greatly increases this induction period versus the corresponding amine complexes, (40 min and 92 min vs. 24 min and 49 min). Surprisingly, while the presence of the methyl on the imidazole had little effect on the spectroscopic or electrochemical properties of the complexes, it leads to a substantial decrease in the activation period compared to the

non-methylated derivative (24 min for **4** vs 49 min for **3** and 40 min for **2** vs 92 min for **1**). It was also observed that the presence of the pyridine moiety greatly reduces the activation period as shown by the comparison of **6** with **3** and **4** (10 min vs. 49 min and 24 min respectively) as well as between **7** and **5** (3 min vs. 19 min). The use of a 2-position linked imidazole also appears to slightly reduce the lag time as seen in comparing **4** (24 min) and **5** (19 min). The same trend is observed for the maximum reaction speed: the use of a pyridine or a 2-position imidazole gives a greater maximum conversion rate than the 4-position imidazole. The presence of an amine function in place of an imine and the N-methylation of the imidazole both slightly increase the rate. These observations together are coherent with **7** having the shortest lag time and the highest conversion rate.

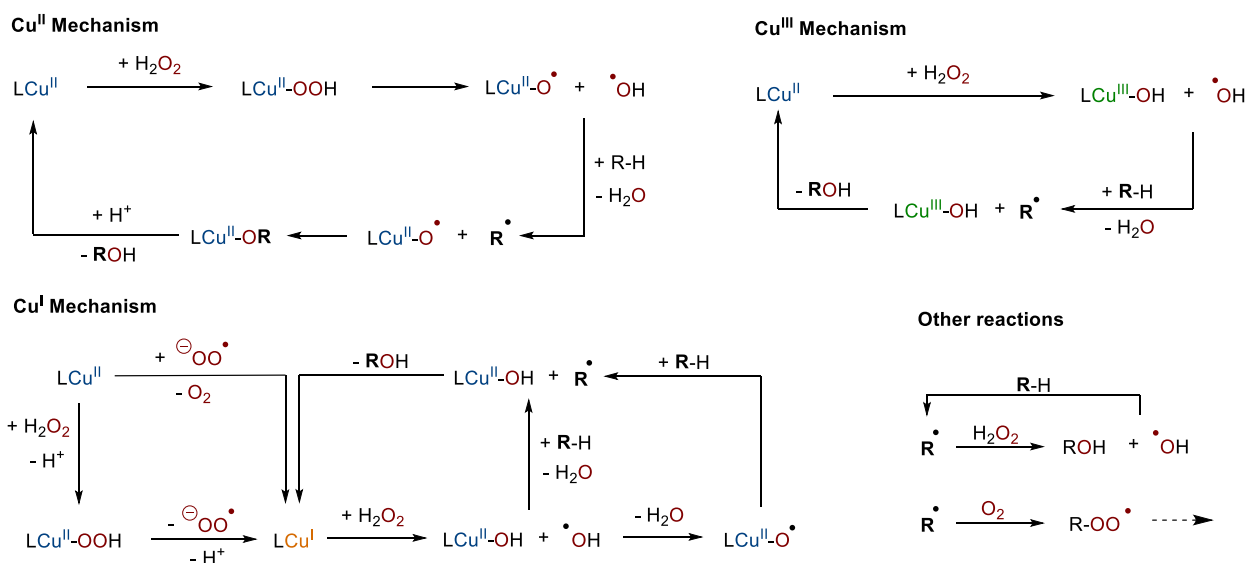
It should be noted that the counter-ion (ClO_4^- vs Cl^-) has a low impact on the catalytic assay, the assay of perchlorate containing compound **5** in presence of 1 or 10 equivalents of chloride did not lead to any significant variations, further supporting the limited association of the counterions as seen in the electrochemical studies. Globally, for the amine linker complexes, the lag time is inversely correlated with the reduction potentials of the compounds recorded in MeOH, i.e. the more easily reduced compounds display the fastest onset times. When CVs were recorded in the buffer solution used for the catalytic assays (**Figure S36** and **Table S9**) the correlation was better, with the ease of reduction for compounds **2-7** matching the order of their induction periods, though **1** remained anomalous (**Figure S37**).

To further look into the reactivity, the four best performing compounds, complexes **4 – 7**, were mixed with hydrogen peroxide in the absence of PNPg and the UV-visible spectra were recorded. A new species with an absorption band at 305 nm was observed, which then decays over approximately 15 minutes (**Figures S44**). The species still displays the typical d-d transition around 650 nm consistent with a Cu(II) complex, and based on previous reports,²⁸ the band at 305 nm is assigned to a LMCT transition of a Cu(II)OOH intermediate. This intermediate forms during the induction times observed for the compounds, though builds up slightly faster for **5** than for **6**, opposite to their respective induction periods (**Figure S45**). However, the intensity of the absorption band as well as its decay in the absence of PNPg correlate well with the maximum

speeds recorded in the catalytic assays, i.e. **5** and **7** have faster maximum rates, while **6** and **4** are similar.

The formation and decay of the intermediate also coincide with production of hydroxyl radicals. Coumarin-3-carboxylic acid was used as a hydroxyl radical trap under the conditions of the catalytic assays but without PNPg. The formation of 7-hydroxycoumarin-carboxylic acid was followed by fluorescence spectroscopy, monitoring the emission at 447 nm, hydroxyl radical production is evidenced with all of the complexes (**Figure 3** center and **Figure S46**). Moreover, like for the assays with PNPg, sigmoidal kinetics are also observed for the production of hydroxyl radicals, with the induction periods being similar to what is observed for the onset of p-nitrophenolate production and correlated with the decay of the proposed Cu(II)OOH species, **Figure 3** bottom. This suggests that hydroxyl radicals produced by the complexes are the main agent responsible for the degradation of PNPg. Competition studies with PNPg and Coumarin-3-carboxylic acid further support this free radical mechanism (**Figure S47**). In the presence of the coumarin (PNPg: Coumarin = 4:1), the formation of para-nitrophenolate over 2 hours is decreased by more than 50%.

The production of hydroxyl radicals from copper complexes or salts is well known in the literature and different mechanisms have been proposed involving different Cu oxidation states for their formation and reaction with substrates, **Scheme 3**. With only Cu(II), (*Cu(II) mechanism*), direct homolytic O-O bond cleavage of in a Cu(II)-OOH species can occur to give a Cu(II)-O[•] and HO[•], followed by H atom abstraction from the substrate, R-H, to give R[•].^{22,45} In the simplest metal centered termination, recombination with Cu(II)-O[•] and protonation provides the hydroxylated product and the starting Cu(II). Alternatively, (*Cu(I) mechanism*) reduction of Cu(II) to Cu(I), either by homolytic Cu-O bond cleavage or by another species in solution can allow for Fenton-like chemistry,⁴⁵ where Cu(I) reacts with H₂O₂ to give Cu(II)-OH and HO[•]. The hydroxy radical can do the H-atom abstraction followed by rebound with the Cu(II)-OH to give the oxidized product and a Cu(I), or the HO[•] abstracts an H-atom from Cu(II)-OH to give Cu(II)-O[•] which then does the abstraction from the substrate. The latter is proposed as a mechanism for LPMOs when hydrogen peroxide is the oxygen cosubstrate.⁴⁶ Additionally, a *Cu(III) mechanism* has been described involving similar Fenton like steps as for the Cu(I) mechanism.^{47,48}



Scheme 3: Mechanisms for hydroxyl radical production and substrate (R-H) activation that have been proposed for copper complexes.⁴⁵⁻⁴⁷

For the model complexes described in this work, the Cu(II)/Cu(III) mechanism is excluded based on the electrochemical results. Additionally, the simplest Cu(II) mechanism involving recombination and reforming of the starting Cu(II) complex would not explain the induction periods observed, as the initial slow step would occur in each cycle. Rather, the induction period suggests that there is either a slow activation of the complexes to give the catalytically active species or that once the reaction begins, one of the products or intermediates can activate the complex or otherwise propagate a chain reaction.⁴⁹ For the Cu(II) mechanism, this could still involve the initial production of the hydroxyl radicals and H-atom abstraction, with the substrate radical going on to react with O₂ to give an organic peroxy radical capable of another H-atom abstraction, or, for PNPG, the substrate radical could react with H₂O₂ to generate another equivalent of HO[•]. Still, while such chain reaction descriptions could be suitable for PNPG, where H-atom abstraction is the crucial mechanistic step, the possibility of propagation of the reaction of hydroxyl radicals with coumarin-3-carboxylic acid is less clear.⁵⁰ Based on this, the activation of the complexes to give a more reactive species is the most likely possibility and would be consistent with the observed build-up and decomposition of the intermediate species preceding HO[•] production. The nature of the active structure, and whether it is a Cu(II) or Cu(I) complex, remains to be determined. However, as the induction periods correlate with the ease of reduction of the complexes, it is possible that the decay of the intermediate may involve the formation of a Cu(I) complex and a subsequent Fenton-like mechanism. The reduction could come from either homolytic cleavage of the Cu-O bond in a Cu-OOH intermediate or by one of the radical species generated by either an initial Cu(II) mechanism or a

Fenton-like mechanism with residual copper salts in solution. Indeed, nanomolar concentrations of Cu(II) salts have been shown to promote Fenton-like chemistry, with the Cu(II) ion being reduced by H₂O₂,^{51,52} and the presence of this amount of free Cu(II) cannot be ruled out. To look at the possibility of reduction of the Cu(II) complexes, ascorbic acid was added to the assays with the coumarin-3-carboxylic acid (**Figures S48 and S49**). The results are complicated to interpret as ascorbate alone can reduce H₂O₂, leading to formation of 7-hydroxycoumarin-carboxylic acid over ten minutes. However, in the presence of the complexes and ascorbate, the addition of H₂O₂ leads to nearly an equal amount of 7-hydroxycoumarin-carboxylic acid in the time required for mixing the sample (<1 minute). While the presence of ascorbate is less relevant to the reducing species that would be present in the PNPG or coumarin-3-carboxylic acid reactions, this nevertheless suggests that the reduction to a Cu(I) species may indeed be important for the reactivity observed for the complexes.

Conclusions

The importance of the histidine brace for copper biochemistry can be seen in its prevalence in different enzymes. In addition to LPMO, it has also been observed in particulate methane monooxygenase,⁵³ copper-binding protein CopC,⁵⁴ spindles of the fusolin protein produced by entomopoxviruses,⁵⁵ and fungal protein Bim 1⁵⁶, highlighting a range of roles for this coordination motif. In this work, we have described the synthesis and characterization of a series of copper imidazole complexes based on N3 ligands related to the histidine brace, which display variation in the methylation of the imidazole rings, the 2-/4-connectivity of the imidazole, the amine/imine nature of the linker, and presence of a pyridine vs imidazole.

The compounds show similar T-shaped N3 coordination as in LPMOs and display similar EPR and UV-vis spectroscopic properties. Still, the structural variations have moderate effects on the electrochemical properties in MeOH. The presence of a pyridine in the complexes overshadows the other changes leading to the largest positive shifts for the Cu(II)/Cu(I) reduction. Nevertheless, while methylation has little influence on the reduction potential, both the 2-connected imidazoles and imines also displayed more positive reductions than the amine linker 4-connected imidazole derivatives, **3** and **4**. This is particularly interesting in the case of the connectivity of the imidazoles as it suggests important differences in the donor/acceptor strengths of these units.

The oxidative reactivity of the compounds was tested with the PNPG assay and also showed structure dependent behavior. Unlike previous LPMO models, all of the complexes described in this work show sigmoidal kinetics for the degradation of the substrate, with lag times for the compounds ranging between 3-90 minutes prior to product formation. Importantly, the lag times allowed to relate the PNPG reactivity with both the formation and decay of an intermediate resulting from reaction of H₂O₂ with the complexes and the time observed for hydroxyl radical production using coumarin-3-carboxylic acid as a hydroxyl radical trap. This provides good support for a free radical mechanism being the main pathway for the PNPG degradation in the case of these complexes.

Experimental

Chemicals and synthesis. All commercial reagents and solvents were obtained from Sigma-Aldrich, Acros Organics or Fluorochem, and were used as purchased without further purification unless otherwise stated. Dry solvents were obtained by standard procedures according to D. D. Perrin and D. R. Perrin, Purification of Laboratory Chemicals. Tetrahydrofuran and diethylether were purified by distillation from benzophenone ketyl radical. Dichloromethane, toluene, trimethylamine and trimethylsilyl chloride were purified by distillation from calcium hydride. Technical grade ethyl acetate and petroleum ether (40 to 65 °C fraction) were distilled under reduced pressure. Analytical thin layer chromatography (TLC) was carried out on Merck Millipore F254 silica gel 60 plates (210-270 μm thickness, aluminium supported). The plates were visualized using ultra-violet light (254 nm). Flash column chromatography was carried out on ROCC silica gel 60Å (230-400 Mesh). N-methyl-histamine and 1-trityl-imidazole-4-carboxaldehyde were synthesized through modified reported procedures described in the SI. The detailed procedures and characterizations of ligands 3-7 and complexes 1-7 are further described in the SI. **Caution!** Copper perchlorate is category 2 oxidizing solid and potentially explosive. All due precautions should be taken.

Synthesis of L3. The suspension of L3Tr (1 g, 2.31 mmol, 1 eq.) in aqueous HCl (40 mL, 1M) was stirred at room temperature overnight. The resulting suspension was filtered and the filtrate was evaporated under vacuum to afford L3 as a white powder (0.566 g, 93%) 1H NMR (300 MHz, d₆-DMSO) δ (ppm): 9.16 (d, J

= 1.2 Hz, 1H), 9.07 (d, J = 1.3 Hz, 1H), 7.88 (s, 1H), 7.58 (s, 1H), 4.34 (s, 2H), 3.35 – 3.28 (m, 2H), 3.22 – 3.14 (m, 3H). 13C NMR (75 MHz, d₆-DMSO) δ (ppm): 134.90, 134.41, 128.99, 124.54, 121.01, 117.39, 44.72, 21.36.

Synthesis of L4. The suspension of L4Tr (0.75 g, 1.67 mmol, 1 eq.) in aqueous HCl (40 mL, 1M) was stirred at room temperature overnight. The resulting suspension was filtered and the filtrate was evaporated under vacuum to afford the product as a white powder (0.401 g, 86%). 1H NMR (300 MHz, d₆-DMSO) δ (ppm): 9.14 (d, J = 1.2 Hz, 1H), 9.05 (d, J = 0.7 Hz, 1H), 7.88 (d, J = 1.0 Hz, 1H), 7.60 (d, J = 1.0 Hz, 1H), 4.33 (s, 2H), 3.82 (s, 3H), 3.29 (t, J = 7.3 Hz, 2H), 3.20 – 3.14 (t, J = 7.3 Hz, 2H). 13C NMR (75 MHz, d₆-DMSO) δ (ppm): 136.00, 134.95, 129.34, 124.53, 121.51, 121.06, 44.80, 35.96, 21.39.

Synthesis of L5. To a solution of 1H-imidazole-2-carbaldehyde (1 g, 10.19 mmol, 1 eq.) and a3 (2.02 g, 10.19 mmol, 1 eq.) in dry methanol (50 mL, dried on 3 Å molecular sieves) under argon were added 3 Å activated molecular sieves and sodium hydroxide (0.774 g, 19.36 mmol, 1.9 eq.). The solution was stirred 2h at room temperature and NaBH₄ (0.771 g, 20.39 mmol, 2 eq.) was added. After 3h at room temperature the mixture was filtered and evaporated under vacuum. The resulting solid was suspended in water (100 mL) and extracted with dichloromethane (3 x 75 mL) and followed with a solution of isopropanol (25%) in chloroform (3 x 100 mL). The isopropanol phases were gathered, dried on Na₂SO₄ and evaporated under vacuum to afford the product L5 as a white solid (1.129 g, 55%). 1H NMR (300 MHz, d₆-DMSO) δ (ppm): 7.42 (d, J = 0.7 Hz, 1H), 6.87 (s, 1H), 6.80 (s, 1H), 3.69 (s, 2H), 3.57 (s, 3H), 2.70 (t, J = 6.9 Hz, 2H), 2.55 (t, J = 7.1 Hz, 2H). 13C NMR (75 MHz, d₆-DMSO) δ (ppm): 147.59, 140.47, 137.54, 117.19, 49.48, 46.95, 33.12, 28.81. HRMS (ESI) : m/z calculated for C₁₀H₁₆N₅ [M+H]⁺ 206.14002, found 206.13987

Synthesis of L6Tr. To a solution of a4 (0.554 g, 1.637 mmol, 1 eq.) and 2-pyridylethylamine (0.2 g, 1.637 mmol, 1 eq.) in dry methanol (25 mL, dried on 3 Å molecular sieves) under argon were added 3 Å activated molecular sieves and sodium acetate (0.134 g, 1.637 mmol, 1 eq.). The solution was stirred 4h at room temperature and NaBH₄ (0.124 g, 3.274 mmol, 2 eq.) was added. After 2h at room temperature the mixture was filtered and evaporated under vacuum. The resulting solid was suspended in water (75 mL) and extracted with dichloromethane (3 x 75 mL), the organic phases were gathered, dried on Na₂SO₄ and evaporated under vacuum. The crude product was purified over flash silica gel chromatography (Methanol-NH₃ (7N)/DCM, 3:97) to afford the product L6Tr as a white solid (0.314 g, 43%). 1H NMR (300 MHz, d₆-DMSO) δ (ppm): 8.42 (ddd, J = 4.9, 1.8, 0.9 Hz, 1H), 7.64 (td, J = 7.6, 1.9 Hz, 1H), 7.45 – 7.35 (m, 9H), 7.27 (d, J = 1.4 Hz, 1H), 7.17 (ddd, J = 8.4, 6.0, 4.5 Hz, 2H), 7.12 – 7.04 (m, 6H), 6.69 (d, J = 1.1 Hz, 1H), 3.56 (s, 2H), 2.82 (s, 4H). 13C NMR (75 MHz, d₆-DMSO) δ (ppm): 160.78, 149.39, 142.86, 140.65, 138.19, 136.80, 129.72, 128.72, 128.49, 123.55, 121.73, 118.85, 74.92, 49.06, 47.18, 38.28. HRMS (ESI) : m/z calculated for C₃₀H₂₉N₄ [M+H]⁺ 445.2392, found 445.2394.

Synthesis of L6. The suspension of L6Tr (0.314 g, 0.706 mmol, 1 eq.) in aqueous HCl (15 mL, 1M) was stirred at room temperature overnight. The resulting suspension was filtered and the filtrate was evaporated under vacuum to afford the product L6 as a white powder (0.194 g, quantitative). ¹H NMR (300 MHz, d₆-DMSO) δ (ppm): 10.27 (s, 2H), 9.16 (d, J = 1.3 Hz, 1H), 8.76 (dd, J = 5.5, 0.9 Hz, 1H), 8.35 (td, J = 7.8, 1.3 Hz, 1H), 7.95 – 7.84 (m, 2H), 7.79 (d, J = 6.5 Hz, 1H), 4.36 (s, 2H), 3.53 – 3.41 (m, 4H). ¹³C NMR (75 MHz, d₆-DMSO) δ (ppm): 152.92, 145.64, 143.12, 134.98, 127.79, 125.74, 124.54, 121.05, 44.91, 39.57, 31.24. HRMS (ESI) : m/z calculated for C₁₁H₁₅N₄ [M+H]⁺ 203.1297, found 203.1296

Synthesis of L7. To a solution of 1-methyl-2-imidazolecarboxaldehyde (0.1 g, 0.908 mmol, 1 eq.) and 2-pyridylethylamine (0.111 g, 0.108 mL, 0.908 mmol, 1 eq.) in dry methanol (10 mL, dried on 3 Å molecular sieves) under argon were added 3 Å activated molecular sieves and sodium acetate (0.075 g, 0.908 mmol, 1 eq.). The solution was stirred 3h at room temperature and NaBH₄ (0.069 g, 1.816 mmol, 2 eq.) was added. After 2h at room temperature the mixture was filtered and evaporated under vacuum. The resulting solid was suspended in a saturated bicarbonate aqueous solution (50 mL) and extracted with dichloromethane (3 x 50 mL). The organic phases were gathered, dried on Na₂SO₄ and evaporated under vacuum. The crude was purified over flash silica gel chromatography (Methanol/Net3/DCM, 5:1:94) to afford the product L7 as a white solid (0.097 g, 50%). ¹H NMR (300 MHz, CDCl₃) δ (ppm): 8.55 – 8.48 (m, 1H), 7.58 (td, J = 7.7, 1.8 Hz, 1H), 7.19 – 7.06 (m, 2H), 6.90 (d, J = 1.1 Hz, 1H), 6.79 (d, J = 1.0 Hz, 1H), 3.87 (s, 2H), 3.61 (s, 3H), 3.10 – 3.01 (m, 2H), 3.02 – 2.92 (m, 2H).

Synthesis of 1. 1H-Imidazole-4-carbaldehyde (0.097 g, 1.1 mmol, 1 eq.), histamine dihydrochloride (0.186 g, 1.1 mmol, 1 eq.) and copper perchlorate hexahydrate (0.374 g, 1.1 mmol, 1 eq.) were dissolved in MeOH (6 mL). The mixture was stirred at room temperature overnight. The resulting suspension was cooled down to 0°C and filtered. The solid was collected, triturated in diethyl ether, filtered and dried under vacuum to afford the complex 1 as a blue powder (0.141 g, 33%). HRMS (ESI) m/z calculated for C₉H₁₁ClCuN₅ [M + Cl]⁺ 286.99990, found 286.99924. Elemental analysis: Calculated for C₉H₁₁N₅Cl₂CuO₄, C, 27.88; H, 2.86; N, 18.07. Found C, 27.96; H, 2.84; N, 18.02

Synthesis of 2. 1H-Imidazole-4-carbaldehyde (0.097 g, 1.1 mmol, 1 eq.), a3 (0.2 g, 1.1 mmol, 1 eq.) and copper perchlorate hexahydrate (0.374 g, 1.1 mmol, 1 eq.) were dissolved in MeOH (6 mL). The mixture was stirred at room temperature overnight. The resulting suspension was cooled down to 0°C and filtered. The solid was collected, triturated in diethyl ether, filtered and dried under vacuum to afford the complex 2 as a blue powder (0.159 g, 36%). HRMS (ESI) m/z calculated for C₁₀H₁₃ClCuN₅ [M+Cl]⁺ 301.01555, found 301.01495, m/z calculated for C₁₁H₁₄CuN₅O₂ [M+Formiate]⁺ 311.04435, found 311.04378.

Elemental analysis: Calculated for C₁₀H₁₃N₅Cl₂CuO₄, C, 29.9; H, 3.26; N, 17.44. Found C, 29.9; H, 3.25; N, 17.17

Synthesis of 3. L1 (0.136 g, 0.711 mmol, 1 eq.) and copper perchlorate hexahydrate (0.263 g, 0.711 mmol, 1 eq) were dissolved in MeOH (4 mL). The mixture was stirred overnight at room temperature, diethylether was then added to the crude and a blue powder was filtered. Slow diffusion of ether in a methanol solution of the complex yielded the pure compound 3 (0.55 g, 20%). HRMS (ESI): m/z calculated for C₉H₁₃N₅ClCu [M+Cl]⁺ 289.01555, found 289.01485. Elemental analysis: Calculated for C₉H₁₃N₅Cl₂CuO₄.H₂O, C, 26.51; H, 3.71; N, 17.18. Found C, 26.33; H, 3.36; N, 16.38

Synthesis of 3Tr. L3Tr (0.1 g, 0.231 mmol, 1 eq.) and copper chloride anhydrous (0.031 g, 0.231 mmol, 1 eq) were dissolved in 3 mL of a acetonitrile/MeOH mixture (5:1 v/v). The mixture was stirred at room temperature, after 5 minutes KPF6 (0.085 g, 0.462 mmol, 2 eq.) was added and the resulting suspension was stirred at room temperature for 5 minutes. The precipitate was filtered and ether (100 mL) was added to the filtrate. The resulting suspension was filtered and washed with ether to yield the complex 3Tr as a blue powder (0.154 g, 98%). HRMS (ESI): m/z calculated for C₂₈H₂₇N₅CuCl [M+Cl]⁺ 531.12455, found 531.12472

Synthesis of 4. L4 (0.2 g, 0.447 mmol, 1 eq.) and copper perchlorate hexahydrate (0.16 g, 0.447 mmol, 1 eq) were dissolved in MeOH (2 mL). The mixture was stirred at room temperature, after 2h triethylamine (0.09 g, 0.894 mmol, 2 eq.) was added and the suspension filtered. The solid was resuspended in methanol and trifluoroacetic acid was added (0.102 g, 0.894 mmol, 2 eq.), the resulting solution was stirred 2h at room temperature then evaporated under vacuum. Slow diffusion of ether in a methanol solution of the complex yielded the pure compound 4 (0.255 g, 37%). HRMS (ESI): m/z calculated for C₁₀H₁₅N₅CuCl [M+Cl]⁺ 303.03120, found 303.03073. Elemental analysis: Calculated for C₁₀H₁₅N₅Cl₂CuO₄, C, 29.75; H, 3.75; N, 17.35. Found C, 29.86; H, 3.72; N, 17.05

Synthesis of 5. L5 (0.1 g, 0.487 mmol, 1 eq.) and copper perchlorate hexahydrate (0.181 g, 0.487 mmol, 1 eq) were dissolved in MeOH (2 mL). The mixture was stirred 4h at 60°C then room temperature overnight. Diethylether was then added to the crude and the solution was filtered to afford the complex 5 as a blue crystalline powder (0.120 g, 48%). HRMS (ESI): m/z calculated for C₁₀H₁₅N₅Cu [M-H]⁺ 267.05397, found 267.05389. Elemental analysis: Calculated for C₁₀H₁₅N₅Cl₂CuO₈.2H₂O, C, 23.83; H, 3.80; N, 13.90. Found C, 23.43; H, 3.84; N, 13.34

Synthesis of 6. L6 (0.2 g, 0.727 mmol, 1 eq.) and copper perchlorate hexahydrate (0.269 g, 0.727 mmol, 1 eq) were dissolved in MeOH (10 mL). The mixture was stirred overnight at room temperature, diethylether was then added to the crude and a blue powder was filtered. Slow diffusion of ether in a

methanol solution of the complex yielded the pure compound 6 (0.0845 g, 28%). HRMS (ESI): m/z calculated for C₁₁H₁₄N₄Cu [M-H]⁺ 300.02030, found 300.01959. Elemental analysis: Calculated for C₁₁H₁₄N₄Cl₂CuO₄, C, 32.97; H, 3.52; N, 13.98. Found C 32.34; H 3.33; N, 13.81

Synthesis of 7. L7 (0.0972 g, 0.449 mmol, 1 eq.) and copper perchlorate hexahydrate (0.166 g, 0.449 mmol, 1 eq) were dissolved in MeOH (3 mL). The mixture was stirred overnight at room temperature, diethylether was then added to the crude and a blue powder was filtered. Slow diffusion of ether in a methanol solution of the complex yielded the pure compound 7 (0.162 g, 71%). Elemental analysis: Calculated for C₁₃H₂₀N₄Cl₂CuO₉, C, 30.57; H, 3.95; N, 10.97. Found C, 30.31; H, 3.87; N, 10.75

Nuclear magnetic resonance. Proton nuclear magnetic resonance (¹H NMR) spectra were recorded using Bruker Avance II-300 (300 MHz) spectrometers. Carbon nuclear magnetic resonance (¹³C NMR) spectra were recorded using Bruker Avance II-300 (75 MHz) spectrometers. Chemical shifts (δ) are reported in parts per million (ppm) relative to residual solvent peaks: ¹H (CDCl₃ δ ppm = 7.26, d₆-DMSO δ ppm = 2.50, D₂O δ ppm = 4.79, ¹³C (d₆-DMSO δ ppm = 39.5). Coupling constants are reported in Hertz (Hz). Splitting patterns are designed as: s (singlet), d (doublet), t (triplet), q (quartet), and m (multiplet).

High resolution mass spectroscopy. Mass spectra were recorded by the Mass Spectrometry Service of the “asm” platform from the Institute of Condensed Matter and Nanosciences (IMCN) at UCLouvain, using Q-ToF Waters Synapt XS spectrometers with a Thermo Orbitrap Exactive device. The values are given in Dalton.

X-Ray diffraction crystallography. All diffraction data were recorded on a MAR345 image plate using Mo-K α radiation generated by an Incoatec μ S microfocuss source (Montel Mirrors). All crystals were stable and measured at ambient conditions. Data integration and reduction was carried out using the CrysAlisPRO software package, and the implemented absorption correction was applied. The structures were solved by dual space direct methods (SHELXT) and refined against F₂ by SHELXL-2018/3 or 2019/3. All non-hydrogen bonds were refined anisotropically, hydrogen atoms were added in calculated positions and refined in riding mode, with temperature factors 1.2 times higher than their parent atoms (1.5 for methyl hydrogens).

In 1 the perchlorate anion was slightly disordered over two positions (65/35 ratio) with isotropic restraints added for the minor part. Similar disorder is observed for the perchlorate anion in 2 (about 50/50 ratio). 3 crystallizes in a non-centrosymmetric space group and was refined as an inversion twin and overall isotropic and rigid bond restraints were applied to the ligand. In 4 the perchlorate anion is also disordered (80/20 ratio) and isotropic and rigid bond restraints were applied to the minor part. In 5 both perchlorate anions are found disordered (each 67/33 ratio) and geometric restraints as

well as isotropic and rigid bond restraints were applied. For the non-coordinating perchlorate thermal ellipsoids of the minor part were constrained to be equal to the major part. In 6 the ligand is found disordered over two sites (82/18 ratio). Overall the disordered parts appear to be superposed onto each other with minimal deviation from each other, apart from the inverted chirality on the linker N-atom (centrosymmetric space group). The central NH is engaged in a hydrogen bond with a neighbouring Cl (major part); or forms a H-bond to the oxygen of the disordered perchlorate anion (57/43 ratio) for the minor part. The minor part of the ligand is restrained to be geometrically similar to the major part. Isotropic and rigid bond restraints were set up for the disordered ligand and perchlorate anion.

Electron paramagnetic resonance. CW-EPR spectra were recorded at 100 K (frozen solutions), on a Bruker Magnettech ESR5000 EPR spectrometer operating at ~9.5 GHz (X-band). 10–2 M solutions of copper complexes were prepared in methanol. Samples were contained in 4 mm OD quartz tubes closed with PE caps. The EPR spectra were obtained with the following spectrometer settings: microwave power: 20 mW; modulation amplitude: 0.7 mT and modulation frequency: 100 kHz. The number of scans was 4. Data handling was performed on the Bruker ESR Studio version 1.90.0 software. All spectra are shown after baseline correction. The simulations of CW EPR spectra were run with Easyspin 6.0.0⁵⁷ using the ‘pepper’ function with one electron spin $S=1/2$ (Cu unpaired electron). All parameters were optimized using ‘esfit’ function.

UV/Visible spectroscopy. The spectra were recorded on a VWR UV-1600PC Scanning Spectrophotometer equipped with Deuterium/Tungsten Halogen Lamp.

Electrochemistry. The experiments were carried out in a 10 mL three electrode glass cell with a glassy carbon working electrode ($d = 3$ mm), a platinum wire counter electrode, and a Ag+/Ag pseudo reference electrode. Unless otherwise stated, voltammograms were recorded in methanol with 0.1 M tetrabutylammonium perchlorate under an argon atmosphere, at room temperature and at a scan rate of 100 mV/s. Ferrocene was used as an internal standard.

Elemental Analysis (CHNS) was done with ThermoTM FlashSmartTM Elemental Analyzer.

Reactivity assays. A 1 mL UV quartz cuvette was charged using micropipettes, with 500 μ L of catalyst solution (0.1 mM in buffer), 100 μ L of the H₂O₂ solution (400 mM in buffer), 100 μ L of the PNPG solution (100 mM in buffer) and the total volume was brought to 1 mL with buffer. Reference tests were performed without catalyst. In all cases the total volume was brought to 1 mL with carbonate buffer. The reaction mixtures were manually stirred prior to each measurement to prevent the formation of gas bubbles in the cuvette. Quantification of the product (4-nitrophenolate) was performed by measuring the absorbance at 400 nm ($\epsilon = 1.85 \times 10^4$ M⁻¹.cm⁻¹) every minute for the first 20 min, 2 h and after 24 h. Note that for the measurement after 24 h, the catalytic solution was diluted 10

times. The assays were performed at room temperature (20 °C – 25 °C) protected from light.

Computations. Computations have been carried out using the Jaguar 8.5 pseudospectral program package 8 (Jaguar 8.5, Schrodinger, Inc., New York, NY, 2014). All species have been fully geometry optimized, and the Cartesian coordinates are given in the annex. Density Functional Theory (DFT) was applied by the means of the B3LYP functional^{58,59} corrected for dispersion as proposed by Grimme (D3 correction)⁶⁰. The LACV3P basis set as implemented in Jaguar was used for the copper atom and the standard split valence polarized 6-31+G(d) basis set⁶¹ was used for all other atoms. Electronic energies were obtained after corresponding fully analytical single point calculations, at the BP86/6-31+G(d) level of theory. Thermal and entropic contributions to free energy (at 298.15 K) and zero-point energy have been obtained by performing frequency calculations at the B3LYP-D3/6-31+G(d) level of theory.

Author Contributions

The manuscript and the results included were prepared through contributions of all authors. All authors have given approval to the final version of the manuscript.

Conflicts of interest

There are no conflicts to declare.

Data availability

Supporting Information Available. The data supporting this article have been included as part of the Supplementary Information. Further detailed synthetic descriptions, UV-Vis, EPR, electrochemical analyses, and catalytic results are provided in the supporting information. X-ray crystallographic files for **1-6** and **3^{Tr}** are provided in CIF format. CCDC 2369751-2369758 contain the supplementary crystallographic data for this paper. These data can be obtained free of charge from The Cambridge Crystallographic Data Centre via www.ccdc.cam.ac.uk/structures

Acknowledgements

This project has received funding from the European Union's Horizon 2020 research and innovation programme under the Marie Skłodowska-Curie (H2020-MSCA-IF-2016) grant agreement No 753953 for Y.Y.S.L. U.G. was supported through a doctoral fellowship from the *Fonds de la Recherche Scientifique – FNRS* (FNRS-Aspirant). X.M. was supported through a China Scholarship Council fellowship. M.B. was supported through a doctoral fellowship from the *Fonds de la Recherche Scientifique – FNRS* (FNRS-FRIA). Computational resources have been provided by the supercomputing facilities of the Université catholique de Louvain (CISM/UCL) and the Consortium des Équipements de Calcul Intensif en Fédération

Wallonie Bruxelles (CPCI) funded by the *Fonds de la Recherche Scientifique – FNRS* under convention 2.5020.11. We thank the Centre d'Instrumentation & Résonance Magnétique – CIREM (Université libre de Bruxelles – ULB) for providing support and access to its infrastructure. The EPR spectrometer used in this work has been funded by the *Fonds de la Recherche Scientifique – FNRS* (EQP2019-35305690), Innoviris (2019-BRIDGE-5 PhotoCop) and the *Fonds des plateformes* (ULB).

Notes and references

- 1 G. Vaaje-Kolstad, D. R. Houston, A. H. K. Riemen, V. G. H. Eijsink and D. M. F. Van Aalten, *J. Biol. Chem.*, 2005, **280**, 11313–11319.
- 2 G. Vaaje-Kolstad, S. J. Horn, D. M. F. Van Aalten, B. Synstad and V. G. H. Eijsink, *J. Biol. Chem.*, 2005, **280**, 28492–28497.
- 3 P. V. Harris, D. Welner, K. C. McFarland, E. Re, J. C. Navarro Poulsen, K. Brown, R. Salbo, H. Ding, E. Vlasenko, S. Merino, F. Xu, J. Cherry, S. Larsen and L. Lo Leggio, *Biochem.*, 2010, **49**, 3305–3316.
- 4 C. M. Phillips, W. T. Beeson, J. H. Cate and M. A. Marletta, *ACS Chem. Biol.*, 2011, **6**, 1399–1406.
- 5 R. J. Quinlan, M. D. Sweeney, L. Lo Leggio, H. Otten, J. C. N. Poulsen, K. S. Johansen, K. B. R. M. Krogh, C. I. Jørgensen, M. Tovborg, A. Anthonsen, T. Tryfona, C. P. Walter, P. Dupree, F. Xu, G. J. Davies and P. H. Walton, *Proc. Natl. Acad. Sci. U S A*, 2011, **108**, 15079–15084.
- 6 G. Vaaje-Kolstad, Z. Forsberg, J. S. Loose, B. Bissaro and V. G. H. Eijsink, *Curr. Opin. Struct. Biol.*, 2017, **44**, 67–76.
- 7 S. Kim, J. Ståhlberg, M. Sandgren, R. S. Paton and G. T. Beckham, *Proc. Natl. Acad. Sci. U S A*, 2014, **111**, 149–154.
- 8 D. M. Petrović, B. Bissaro, P. Chylenski, M. Skaugen, M. Sørli, M. S. Jensen, F. L. Aachmann, G. Courtade, A. Várnai and V. G. H. Eijsink, *Prot. Sci.*, 2018, **27**, 1636–1650.
- 9 D. M. Petrović, A. Várnai, M. Dimarogona, G. Mathiesen, M. Sandgren, B. Westereng and V. G. H. Eijsink, *J Biol Chem*, 2019, **294**, 15068–15081.
- 10 E. A. Span, D. L. M. Suess, M. C. Deller, R. D. Britt and M. A. Marletta, *ACS Chem. Biol.*, 2017, **12**, 1095–1103.
- 11 T. Tandrup, T. Tryfona, K. E. H. Frandsen, K. S. Johansen, P. Dupree and L. Lo Leggio, *Biochem.*, 2020, **59**, 3347–3358.
- 12 S. Muthuramalingam, D. Maheshwaran, M. Velusamy and R. Mayilmurugan, *J. Catal.*, 2019, **372**, 352–361.
- 13 A. Mendieta, J. R. Álvarez-Idaboy, V. M. Ugalde-Saldívar, M. Flores-Álamo, A. Armenta, G. Ferrer-Sueta and L. Gasque, *Inorg. Chem.*, 2023, **62**, 16677–16690.
- 14 A. A. Hassoon, A. Szorcik, L. Fülöp, Z. I. Papp, N. V. May and T. Gajda, *Dalton Trans.*, 2022, **51**, 17241–17254.
- 15 J. Saikia, V. T. Bhat, L. R. Potnuru, A. S. Redkar, V. Agarwal and V. Ramakrishnan, *ACS Omega*, 2022, **7**, 19131–19140.
- 16 D. Dhar and W. B. Tolman, *J. Am. Chem. Soc.*, 2015, **137**, 1322–1329.
- 17 C. J. Bouchev, D. Y. Shopov, A. D. Gruen and W. B. Tolman, *ACS Omega*, 2022, **7**, 35217–35232.
- 18 C. Citek, J. B. Gary, E. C. Wasinger and T. D. P. Stack, *J. Am. Chem. Soc.*, 2015, **137**, 6991–6994.
- 19 M. Bhadra, J. Y. C. Lee, R. E. Cowley, S. Kim, M. A. Siegler, E. I. Solomon and K. D. Karlin, *J. Am. Chem. Soc.*, 2018, **140**, 9042–9045.
- 20 S. Kim, J. Y. Lee, R. E. Cowley, J. W. Ginsbach, M. A. Siegler, E. I. Solomon and K. D. Karlin, *J. Am. Chem. Soc.*, 2015, **137**, 2796–2799.
- 21 G. Y. Park, M. F. Qayyum, J. Woertink, K. O. Hodgson, B. Hedman, A. A. Narducci Sarjeant, E. I. Solomon and K. D. Karlin, *J. Am. Chem. Soc.*, 2012, **134**, 8513–8524.

- 22 D. E. Diaz, M. Bhadra and K. D. Karlin, *Inorg. Chem.*, 2019, **58**, 13746–13750.
- 23 2A. Kunishita, M. Kubo, H. Sugimoto, T. Ogura, K. Sato, T. Takui and S. Itoh, *J. Am. Chem. Soc.*, 2009, **131**, 2788–2789.
- 24 S. Itoh, *Acc. Chem. Res.*, 2015, **48**, 2066–2074.
- 25 S. Muthuramalingam, K. Anandababu, M. Velusamy and R. Mayilmurugan, *Inorg. Chem.*, 2020, **59**, 5918–5928.
- 26 I. Castillo, A. C. Neira, E. Nordlander and E. Zeglio, *Inorganica Chim. Acta*, 2014, **422**, 152–157.
- 27 A. C. Neira, P. R. Martínez-Alanis, G. Aullón, M. Flores-Alamo, P. Zerón, A. Company, J. Chen, J. B. Kasper, W. R. Browne, E. Nordlander and I. Castillo, *ACS Omega*, 2019, **4**, 10729–10740.
- 28 A. L. Concia, M. R. Beccia, M. Orio, F. T. Ferre, M. Scarpellini, F. Biaso, B. Guigliarelli, M. Réglier and A. J. Simaan, *Inorg. Chem.*, 2017, **56**, 1023–1026.
- 29 R. Leblay, R. Delgadillo-Ruíz, C. Decroos, C. Hureau, M. Réglier, I. Castillo, B. Faure and A. J. Simaan, *ChemCatChem*, 2023, **15**, 2008, **18**, 1702–1707.
- 30 A. Fukatsu, Y. Morimoto, H. Sugimoto and S. Itoh, *Chem. Comm.*, 2020, **56**, 5123–5126.
- 31 M. G. Saulnier, D. B. Frennesson, M. D. Wittman, K. Zimmermann, U. Velaparthy, D. R. Langley, C. Struzynski, X. Sang, J. Carboni, A. Li, A. Greer, Z. Yang, P. Balimane, M. Gottardis, R. Attar and D. Vyas, *Bioorg. Med. Chem. Lett.*, 2008, **18**, 1702–1707.
- 32 S. Durmus, J. C. Garrison, M. J. Panzner, C. A. Tessier and W. J. Youngs, *Tetrahedron*, 2005, **61**, 97–101.
- 33 J. Ohkanda, J. W. Lockman, M. A. Kothare, Y. Qian, M. A. Blaskovich, S. M. Sebti and A. D. Hamilton, *J. Med. Chem.*, 2002, **45**, 177–188.
- 34 K. E. H. Frandsen, J. C. N. Poulsen, T. Tandrup and L. Lo Leggio, *Carbohydr. Res.*, 2017, **448**, 187–190.
- 35 M. Gudmundsson, S. Kim, M. Wu, T. Ishida, M. H. Momeni, G. Vaaje-Kolstad, D. Lundberg, A. Royant, J. Ståhlberg, V. G. H. Eijsink, G. T. Beckham and M. Sandgren, *J. Biol. Chem.*, 2014, **289**, 18782–18792.
- 36 V. V. Vu and S. T. Ngo, *Coord. Chem. Rev.*, 2018, **368**, 134–157.
- 37 W. A. Alves, R. H. De Almeida Santos, A. Paduan-Filho, C. C. Becerra, A. C. Borin and A. M. Da Costa Ferreira, *Inorganica Chim. Acta.*, 2004, **357**, 2269–2278.
- 38 M. Scarpellini, A. Neves, R. Hörner, A. J. Bortoluzzi, B. Szpoganics, C. Zucco, R. A. Nome Silva, V. Drago, A. S. Mangrich, W. A. Ortiz, W. A. C. Passos, M. C. B. De Oliveira and H. Terenzi, *Inorg. Chem.*, 2003, **42**, 8353–8365.
- 39 A. Okuniewski, D. Rosiak, J. Chojnacki and B. Becker, *Polyhedron*, 2015, **90**, 47–57.
- 40 A. W. Addison, T. N. Rao, J. Reedijk, J. Van Rijn and G. C. Verschoor, *J. Chem. Soc., Dalton Trans.*, 1984, 1349–1356.
- 41 H. Golchoubian, O. Nazari and B. Kariuki, *J. Chin. Chem. Soc.*, 2011, **58**, 60–68.
- 42 R. Horikoshi, Y. Funasako, T. Yajima, T. Mochida, Y. Kobayashi and H. Kageyama, *Polyhedron*, 2013, **50**, 66–74.
- 43 L.-S. Long, S.-P. Yang, Y.-X. Tong, Z.-W. Mao, X.-M. Chen and L.-N. Ji, *J. Chem. Soc., Dalton Trans.*, 1999, 1999–2004.
- 44 T. P. Mohammed, A. George, M. P. Sivaramkrishnan, P. Vadivelu, S. Balasubramanian and M. Sankaralingam, *J. Inorg. Biochem.*, 2023, **247**
- 45 S. Kim, J. W. Ginsbach, J. Y. Lee, R. L. Peterson, J. J. Liu, M. A. Siegler, A. A. Sarjeant, E. I. Solomon and K. D. Karlin, *J. Am. Chem. Soc.*, 2015, **137**, 2867–2874.
- 46 B. Bissaro, Å. K. Røhr, G. Müller, P. Chylenski, M. Skaugen, Z. Forsberg, S. J. Horn, G. Vaaje-Kolstad and V. G. H. Eijsink, *Nat. Chem. Biol.*, 2017, **13**, 1123–1128.
- 47 I. Garcia-Bosch and M. A. Siegler, *Angew. Chem.*, 2016, **128**, 13065–13068.
- 48 M. Yamada, K. D. Karlin and S. Fukuzumi, *Chem. Sci.*, 2016, **7**, 2856–2863.
- 49 P. Ulanski and C. Von Sonntag, *J. Chem. Soc., Perkin Trans. 2*, 1999, 165–168.
- 50 G. Louit, S. Foley, J. Cabillic, H. Coffigny, F. Taran, A. Valleix, J. P. Renault and S. Pin, *Radiat. Phys. and Chem.*, 2005, **72**, 119–124.
- 51 Leidi Cecilia Friedrich, Carmem Lúcia de Paiva e Silva Zanta, Amilcar Machulek Jr, Volnir de Oliveira Silva and Frank Herbert Quina, *Sci. Agric.*, 2012, **69**, 347–351.
- 52 A. N. Pham, G. Xing, C. J. Miller and T. D. Waite, *J. Catal.*, 2013, **301**, 54–64.
- 53 L. Cao, O. Caldararu, A. C. Rosenzweig and U. Ryde, *Angew. Chem.*, 2018, **130**, 168–172.
- 54 J. Ipsen, C. Hernández-Rollán, S. J. Munderspach, S. Brander, A. B. Bertelsen, P. E. Jensen, M. H. H. Nørholm, L. Lo Leggio and K. S. Johansen, *FEBS Lett.*, 2021, **595**, 1708–1720.
- 55 E. Chiu, M. Hijnen, R. D. Bunker, M. Boudes, C. Rajendran, K. Aizel, V. Oliéric, C. Schulze-Briese, W. Mitsuhashi, V. Young, V. K. Ward, M. Bergoin, P. Metcal and F. Coulibaly, *Proc. Natl. Acad. Sci. U S A*, 2015, **112**, 3973–3978.
- 56 S. Garcia-Santamarina, C. Probst, R. A. Festa, C. Ding, A. D. Smith, S. E. Conklin, S. Brander, L. N. Kinch, N. V. Grishin, K. J. Franz, P. Riggs-Gelasco, L. Lo Leggio, K. S. Johansen and D. J. Thiele, *Nat. Chem. Biol.*, 2020, **16**, 337–344.
- 57 S. Stoll and A. Schweiger, *J. Magn. Reson.*, 2006, **178**, 42–55.
- 58 A. D. Becke, *J. Chem. Phys.*, 1993, **98**, 5648–5652.
- 59 P. J. Stephens, F. J. Devlin, C. F. Chabalowski and M. J. Frisch, *J. Phys. Chem.*, 1994, **98**, 11623–11627.
- 60 S. Grimme, J. Antony, S. Ehrlich and H. Krieg, *J. Phys. Chem.*, 2010, **132**
- 61 W. J. Hehre and W. A. Lathan, *J. Chem. Phys.*, 1972, **56**, 5255–5257.